

Upscaling scheme for long-term ion diffusion in charged porous media

Yuankai Yang and Moran Wang*

Department of Engineering Mechanics and CNMM, Tsinghua University, Beijing 100084, China

(Received 19 February 2017; published 25 August 2017)

Description of long-term (over years) ion diffusion at the pore scale is a huge challenge since the characteristic time of diffusion in a typical representative elementary volume is around microseconds, generally ten orders of magnitude lower than the time we were concerned with. This paper presents a numerical upscaling scheme for ion diffusion with electrical double-layer effects (electrodifusion) considered in charged porous media. After a scaling analysis for the nondimensional governing equations of ion transport at the pore scale, we identify the conditions for decoupling of electrical effect and diffusion, and therefore are able to choose apposite temporal and spatial scales for corresponding directions of the electrodiffusion process. The upscaling scheme is therefore proposed based on a numerical framework for governing equations using a lattice Boltzmann method. The electrical potential or concentration profiles from steady- or unsteady-state electrodiffusion in the long, straight channel, calculated by this upscaling scheme, are compared with the well-meshed full-sized simulations with good agreement. Furthermore, this scheme is used to predict tracer-ion throughdiffusion and outdiffusion in hardened cement pastes. All numerical results show good agreement with the full-sized simulations or experiment data without any fitting parameters. This upscaling scheme bridges the ion diffusion behaviors in different time scales, and may help to improve the understanding of long-term ion transport mechanisms in charged porous media.

DOI: [10.1103/PhysRevE.96.023308](https://doi.org/10.1103/PhysRevE.96.023308)

I. INTRODUCTION

The ion diffusion in charged porous media (e.g., clay and cell) is a fundamental phenomenon in nature. This field of science is promising and has been deeply studied by numerous researchers for its extensive applications such as the transport of heavy ions in soil [1,2], groundwater contamination [3], nuclear waste disposal [4–6], and the marine structure anticorrosion [7–9]. To understand the mechanism of ion diffusion in such charged porous materials, copious experiments were performed and simplified empirical models were proposed to calculate the effective ion diffusion coefficients and to understand the long-term behavior of ion diffusion [6,10–16]. For example, Tachi and Yotsuji [14] and Glaus *et al.* [12] reported the measurements of effective diffusion coefficients and sorption behavior of HTO, Na⁺, and Cl[−] in the compacted montmorillonite. It was observed that the cationic effective diffusion coefficients are higher than anionic. Meanwhile, Glaus *et al.* [15] found through experiments that the salinity and pH in the pore solution could also affect the ion diffusion. To explain these phenomena, the electrical double-layer effect was introduced [17,18]. As well known, the charged surface of clay materials induces an electrical double layer (EDL) in the electrolyte by the long-range Coulomb force and therefore influences the ion distribution in pores. When the EDL thickness is comparable with the pore size, the electrical double-layer effects, including ion-ion and ion-surface interactions, are strong and may play a significant role in ion transport [19–22]. Like compacted bentonite, the most probable pore size of these porous media is nanoscale [23]. Meanwhile the thickness of the EDL is about 1 nm–1.5 μm when the ion concentration ranges from 1 × 10^{−6} to 1 M. Therefore, comparing with the pure diffusion effects, the electrical double-layer effects have a major contribution on the ion diffusion in such compacted

charged porous media. Fundamentally, the macroscale behavior of ion diffusion strongly depends on the surface charge properties at pore scale because of the strong ion-surface interaction. Furthermore, the local solution properties, such as pH, salinity, and so on, could change the surface charge property and the EDL thickness [24–26]. That is why the pH and salinity can change the apparent ion diffusivities. Glaus demonstrated that the effective cationic diffusivity might be significantly underestimated in the absence of the electrical double-layer effects [15]. Therefore, in order to describe the macroscale behavior of ion diffusion in charged porous media, the electrical double-layer effects at pore scale have to be considered very carefully.

Experimental study of long-term ion diffusion in charged porous media is time consuming and challenging in the laboratory, especially when the permeability is very low. Meanwhile the measurements may be dominated by multifactorial coupling (e.g., ionic valence, pH, salinity, etc.) so that it is hard to reveal the real mechanism. Numerical modeling therefore provides an efficient way to help to understand the long-term ionic diffusion process and clarify effects from different factors. Since the pore is usually nanoscale as mentioned above, the characteristic time for ion transport in a typical representative elementary volume (REV) is usually from picosecond to microsecond [27,28]. That is, in order to catch the details of the ion diffusion in the pore-scale numerical modeling, the time interval should be small enough to meet the computing requirements. However, for the practical applications, the time scale is often in the unit of years. For example, the structure durability for cross-sea bridges should be more than 100 years and that for low-level nuclear waste disposal would be more than 300 years. The range of time scale is more than ten orders of magnitude. The typical strategy is using upscaling to overcome this limitation.

Many previous efforts have been reported for upscaling of pore-scale ion transport in charged porous media. In general, there are two avenues: One is to simplify the complex topology

*mrwang@tsinghua.edu.cn

of porous media; the other is implementing homogenization of ion transport in a typical REV to get a macroscale constitutive equation [18]. The former avenue usually translates the geometry of porous media into straight channels [29,30] or pore networks [15,31–33]. For the compacted bentonite (such as Na-montmorillonite), the porosity decrease as the dry bulk density increases. Kozaki *et al.* [30] observed a two-layer hydrate of Na-montmorillonite when the dry bulk density ranges from 1.4 to 1.8 kg/dm⁻³, and Bourg *et al.* [34] introduced a conceptual model in which the pore space is divided into micropore and nanopore parts to study the scale effect for ion transport. Porta *et al.* [29] also presented a continuum-scale model to compute the advection dispersion in the porous media. This model subdivides the total fluid volume into a mobile region and an immobile region. Marconi and Melchionna [35] used a one-dimensional Nernst-Planck description to consider the conductivity in a narrow cylindrical channel of nonuniform shapes. For the pore-network models, it separates the porous media as pore bodies and pore throats, respectively. Li *et al.* [33] and Obliger *et al.* [32] employed pore-network models to assess the influence of the electrokinetic effect on the ion and fluid transport in the porous media. The constitutive equations on their pore-network model are given by Onsager's reciprocal principle. The second avenue is transferring information from the microscale to the macroscale by homogenization methods, including the volume average method [18,36,37], mean-field homogenization [38], and asymptotic expansion method [39,40]. Leroy *et al.* [41] proposed a continuum-scale model, including the effect of the electrical-chemical coupling based on the Donnan equilibrium theory, to estimate the ion diffusion in the bentonite. Afterwards, Jougnot *et al.* [18] developed Leroy's model by the volume average method.

The constitutive equations in these upscaling models need effective parameters (the Onsager's reciprocal coefficients), like effective diffusivity (or conductivity) or fluidic permeability to describe ion transport in charged porous media [35]. Normally these effective coefficients are obtained on steady state. For unsteady ion transport, however, the validity of these effective parameters is doubtful. For instance, the ion diffusivity in charged porous media is dependent on the property of surface charge, but the property of surface charge changes with the local chemical environment as mentioned above. For the unsteady ion transport, the local chemical environment is changing with time and position, so that the surface charge is heterogeneous distribution. It means that the ionic effective diffusivity also changes over time in different positions. In such a situation, it is not very accurate to use the effective diffusivity based on the steady state to calculate the unsteady ion diffusion in charged porous media. Pivonka *et al.* [42] revealed that the classical Donnan theory was based on homogeneous distribution of surface charge, but it might be inconsistent for a heterogeneous distribution situation. Hence for the unsteady ion transport, especially the pore size close to the EDL thickness, the stronger ion-ion and ion-surface interactions could cause more significant nonequilibrium effects [43–46]. Owing to the prior studies using the theories for steady state (e.g., Donnan theory), the unsteady effects may destroy the accuracy [46]. Therefore the

accuracy of prior upscaling methods for unsteady ion transport in porous media is ambiguous [43–45].

The aim of this work is to present an upscaling method for unsteady ion diffusion with electrical double-layer effects in charged channel and porous media. To achieve this aim, the scale analysis and the analogy method are performed on the constitutive equations that govern the process of ion transport. After the analysis, we decouple a two-dimensional ion transport process into several one-dimensional ion transport processes and obtain the upscaling constitutive equations. Finally, we solve these upscaling equations by the lattice Boltzmann method, and the results are compared with well-meshed full-sized simulations and experiment data.

II. UPSCALING SCHEME

The essence of diffusion is thermal motion, and the well-known equation to describe the diffusion is Fick's law. For isotropic media with negligible physical or chemical interactions, the pure ion diffusion is calculated by

$$\frac{\partial C}{\partial t} = \nabla \cdot (D \nabla C), \quad (1)$$

where C and D are the concentration and diffusion coefficient, respectively. With the electrical double-layer effect considered, the mass flux \mathbf{J}_i of the i th ion species is

$$\mathbf{J}_i = -D_i \nabla C_i - \frac{e z_i D_i}{k T} C_i \nabla \psi, \quad (2)$$

where D_i denotes the diffusion coefficient of the i th ion species, C_i the concentration of the i th ion species, ψ the electrical potential, z_i the i th ion algebraic valence, e the absolute charge of electron, k the Boltzmann constant, and T the absolute temperature. The mass flux \mathbf{J}_i and the concentration C_i follow the continuity equation:

$$\frac{\partial C_i}{\partial t} + \nabla \cdot \mathbf{J}_i = 0. \quad (3)$$

Substituting Eq. (2) into Eq. (3) leads to the Nernst-Planck equation.

The ions in pore solution near the surfaces form the electrical double layer, and the electrical potential on the shear plane is called the zeta potential [47], as shown in Fig. 1. The distribution of the electrical potential ψ is governed by the Poisson equation [48]:

$$\nabla^2 \psi = -\frac{\rho_e}{\epsilon_r \epsilon_0} = -\sum_i \frac{N_A e z_i C_i}{\epsilon_r \epsilon_0}, \quad (4)$$

where ρ_e is the net charge density, N_A Avogadro's number, and $\epsilon_r \epsilon_0$ the dielectric constant of the pore solution. Equations (2)–(4) govern the ion transport processes in charged porous media, called the Poisson-Nernst-Planck (PNP) model.

A. Scale analysis

Here we borrow a classical process of scale analysis from the textbook by Lin and Segel [49]. Basically, the scaling means using the apposite scale for the corresponding problem. Herein we employ the scale analysis on the Poisson-Nernst-Planck model. For a two-dimensional long, straight nanochannel, as shown in Fig. 2, with a very high length to

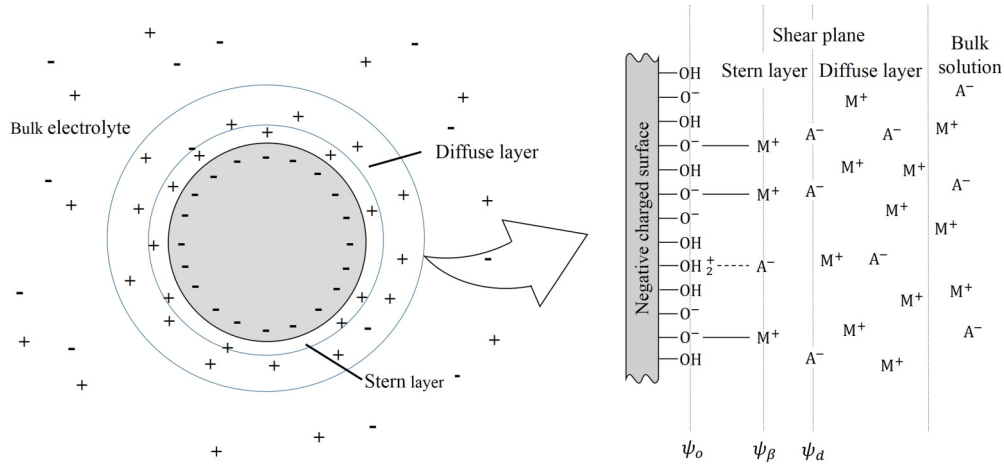


FIG. 1. Sketch of the charged clay particle and electrical double layer [26]. M and A denote the monovalent cation and anion, respectively.

width ratio, the spatial scale is quite different along the x or y directions. As mentioned above, the EDL thickness may be about several nanometers while the channel length can be over several millimeters (or meters). The order of magnitude of the resolution for the spatial scale has a huge gap along different directions, and therefore we have to identify different characteristic lengths for different directions. In this work, there are two spatial scales: One is y^* with the resolution for the EDL thickness in the y direction and the other is x^* to characterize the length of the channel. Hence we define $C_i = C_i^* C_{i,0}$, $x = x^* x_0$, $y = y^* y_0$, $t = t^* t_0$, and $\psi = \psi^* \psi_0$, where C_i^* , x^* , y^* , t^* , and ψ^* are the reference physical units of concentration of the i th ion species, the length along the x and y directions, the time, and the electrical potential, respectively. $C_{i,0}$, x_0 , y_0 , t_0 , and ψ_0 are the dimensionless quantities for the corresponding terms. By substituting these

definitions into Eqs. (2)–(4), the equations are transformed into the dimensionless Poisson-Nernst-Planck equations:

$$\begin{aligned} \frac{1}{D_i t^*} \frac{\partial C_{i,0}}{\partial t_0} &= \frac{1}{(x^*)^2} \frac{\partial^2 C_{i,0}}{\partial x_0^2} + \frac{1}{(y^*)^2} \frac{\partial^2 C_{i,0}}{\partial y_0^2} \\ &+ \frac{z_i e \psi^*}{kT (x^*)^2} \left(\frac{\partial C_{i,0}}{\partial x_0} \frac{\partial \psi_0}{\partial x_0} + C_{i,0} \frac{\partial^2 \psi_0}{\partial x_0^2} \right) \\ &+ \frac{z_i e \psi^*}{kT (y^*)^2} \left(\frac{\partial C_{i,0}}{\partial y_0} \frac{\partial \psi_0}{\partial y_0} + C_{i,0} \frac{\partial^2 \psi_0}{\partial y_0^2} \right), \quad (5) \\ \left(\frac{y^*}{x^*} \right)^2 \frac{\partial^2 \psi_0}{\partial (x_0)^2} + \frac{\partial^2 \psi_0}{\partial (y_0)^2} &= - \sum_i \frac{N_A z_i^2 e C^* (y^*)^2}{\epsilon_0 \epsilon_r \psi^*} (C_{i,0}) z_i^{-1}. \quad (6) \end{aligned}$$

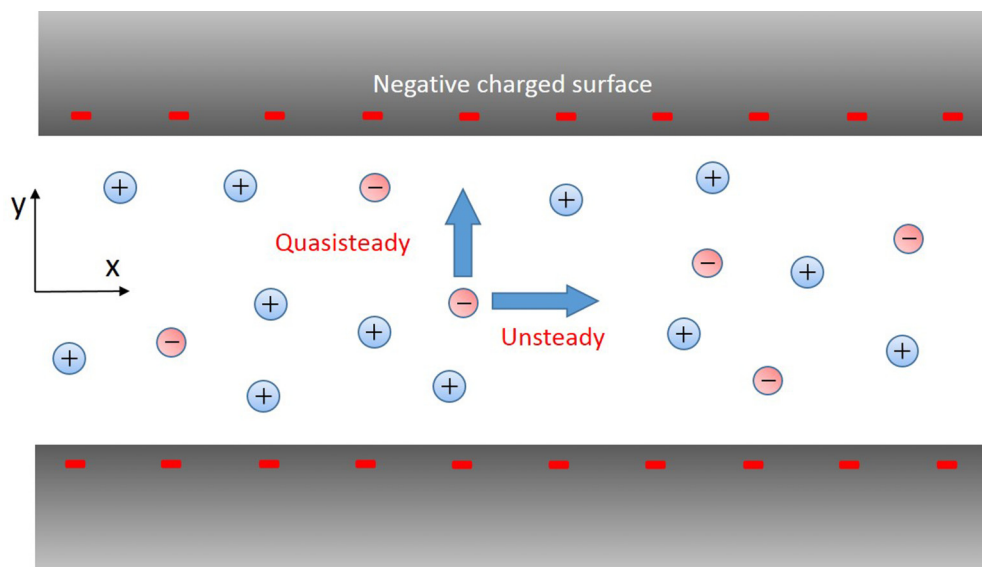


FIG. 2. Sketch of the ion transport in a nanochannel. The gray part is the charged solid surface; the red circle represents the anion and the blue the cation.

In general, for normal mineral surfaces (such as clay, cement), the surface electrical potential (zeta potential) is about -5 to -100 mV [24,50]. Meanwhile, $kT/e = 25.7$ mV for the room temperature. Therefore, $O(e\psi^*/kT) \sim O(1)$ and we define $\psi^* = kT/e$. Furthermore, because mass transport is similar to heat transfer, referring to the Fourier number in heat transfer, we define $t^* = L_i^2/D_i$ so that Eq. (5) can be translated into

$$\begin{aligned} \frac{\partial C_{i,0}}{\partial t_0} &= \frac{L_i^2}{(x^*)^2} \frac{\partial^2 C_{i,0}}{\partial x_0^2} + \frac{L_i^2}{(y^*)^2} \frac{\partial^2 C_{i,0}}{\partial y_0^2} \\ &+ \frac{z_i L_i^2}{(x^*)^2} \left(\frac{\partial C_{i,0}}{\partial x_0} \frac{\partial \psi_0}{\partial x_0} + C_{i,0} \frac{\partial^2 \psi_0}{\partial x_0^2} \right) \\ &+ \frac{z_i L_i^2}{(y^*)^2} \left(\frac{\partial C_{i,0}}{\partial y_0} \frac{\partial \psi_0}{\partial y_0} + C_{i,0} \frac{\partial^2 \psi_0}{\partial y_0^2} \right), \end{aligned} \quad (7)$$

where $C_{i,0}$ is the reference concentration of the i th species. The characteristic electrokinetic length λ_i for the i th species is defined by

$$\lambda_i = \left(\frac{\varepsilon_0 \varepsilon_r k_B T}{N_A z_i^2 e^2 C_{i,0}} \right)^{1/2}. \quad (8)$$

Consider the Debye length λ_D calculated as [51]

$$\lambda_D = \left(\frac{\varepsilon_0 \varepsilon_r k_B T}{\sum N_A z_i^2 e^2 C_{i,0}} \right)^{1/2}, \quad (9)$$

so that the characteristic electrokinetic size λ_i is related to the Debye length λ_D by

$$\frac{1}{\lambda_D^2} = \sum \frac{1}{\lambda_i^2}. \quad (10)$$

The simplified dimensionless Poisson equations are

$$\varepsilon^2 \frac{\partial^2 \psi_0}{\partial (x_0)^2} + \frac{\partial^2 \psi_0}{\partial (y_0)^2} = - \sum_i K_i^2 C_{i,0} z_i^{-1}, \quad (11)$$

where we define $\varepsilon = y^*/x^*$ named the dimensionless spatial scale factor and ε is a small number because x^* is much greater than y^* as noted before. K_i is the dimensionless characteristic electrokinetic size for the i th species defined as

$$K_i^2 = \frac{z_i^2 e^2 N_A C_{i,0} (y^*)^2}{\varepsilon_0 \varepsilon_r k T} = (y^*/\lambda_i)^2. \quad (12)$$

Clearly, the terms $C_{i,0}$ and ψ_0 are coupled with each other and the functional relationships are shown below as

$$C_{i,0} = f(t_0, x_0, y_0, \psi_0, z_i), \quad (13)$$

$$\psi_0 = f(K_i, x_0, y_0, z_i, C_{i,0}). \quad (14)$$

Based on these functional relationships, there are five main dimensionless numbers: t_0 , controlling the schedule of the unsteady ion transport with electrical double-layer effects; K_i , indicating the contribution of the electrical double-layer effect for the i th species; x_0, y_0 , indicating position; and z_i showing ionic electrical property. Thus, so far, the dimensionless Nernst-Planck equation and Poisson equation are given, and then we decouple these equations for different directions.

The left side of Eq. (11) has two terms: $\varepsilon^2 \partial^2 \psi_0 / \partial x_0^2$ and $\partial^2 \psi_0 / \partial y_0^2$, where $\varepsilon^2 \partial^2 \psi_0 / \partial x_0^2$ is much smaller than $\partial^2 \psi_0 / \partial y_0^2$. The reasons are that ε^2 is minute as described above, and the potential gradient along the y direction is usually larger than along the x direction. Therefore $\varepsilon^2 \partial^2 \psi_0 / \partial x_0^2$ is negligible. Equation (11) is thus simplified as

$$\frac{\partial^2 \psi_0}{\partial (y_0)^2} = - \sum_i K_i^2 C_{i,0} z_i^{-1}. \quad (15)$$

After this treatment, the two-dimensional Poisson equation is simplified to a one-dimensional equation. For dilute electrolyte solutions, the ionic concentration of the diffuse layer in the nanochannel matches with the Boltzmann distribution [45,52]:

$$C_{i,0} = C_{i,m} \exp[-z_i(\psi_0 - \psi_{0,m})], \quad (16)$$

where $C_{i,m}$ and $\psi_{0,m}$ denote the ion concentration and electrical potential in the middle of the nanochannel. Substitution of Eq. (16) into Eq. (15) gives the dimensionless Poisson-Boltzmann equation:

$$\frac{\partial^2 \psi_0}{\partial (y_0)^2} = - \sum_i K_i^2 C_{i,m} \exp[-z_i(\psi_0 - \psi_{0,m})] z_i^{-1}. \quad (17)$$

Equation (17) is based on the Poisson-Boltzmann model, so that our model may be not valid for electrolyte solutions with very high salinities (over 1 M) or with outside ions.

For the dimensionless Nernst-Planck equation, actually there are two relaxation times [27,28]. By defining $L_i = y^*$, we can get the first relaxation time, $t_y^* = (y^*)^2/D_i$, which is rather small in the range from nanosecond to microsecond. It means that the ion electrodiffusion along the y direction in the nanochannel is very fast. Note that y^* is the resolution for EDL thickness in the y direction and has the same length scale as the Debye length, which characterizes the EDL thickness. Therefore we can also get $t_y^* \approx \lambda_D^2/D_i$, similar to the time scale suggested by Rubinstein *et al.* [27]. This time scale implies the EDL charging along the y direction with a diffusion coefficient D_i across one Debye screen length. This time scale is also called the Debye relaxation time which corresponds to the relaxation of charge fluctuations. Substitute $L_i = y^*$ into Eq. (7) and note $\varepsilon = y^*/x^* \ll 1$; we can obtain

$$\frac{\partial C_{i,0}}{\partial t_0} = \frac{\partial^2 C_{i,0}}{\partial y_0^2} + z_i \left(\frac{\partial C_{i,0}}{\partial y_0} \frac{\partial \psi_0}{\partial y_0} + C_{i,0} \frac{\partial^2 \psi_0}{\partial y_0^2} \right). \quad (18)$$

This is the dimensionless ion transport equation in the minor time scale. Equation (18) means that the y direction is the dominant ion transport direction when the time scale is in the range from nanosecond to microsecond. In other words, when $\Delta t \gg t_y^* = (y^*)^2/D_i$, $\partial C_{i,0}/\partial t_0 \rightarrow 0$ after Δt time. Because Eq. (18) is a parabolic equation, the convergence rate with the time term of this formula is an exponential relationship as follows:

$$\begin{aligned} \frac{\partial^2 C_{i,0}}{\partial y_0^2} + z_i \left(\frac{\partial C_{i,0}}{\partial y_0} \frac{\partial \psi_0}{\partial y_0} + C_{i,0} \frac{\partial^2 \psi_0}{\partial y_0^2} \right) &\sim O[\exp(-\Delta t/t_y^*)] \\ &\approx 0. \end{aligned} \quad (19)$$

Essentially Eq. (18) implies the process of EDL charging along the y direction in the nanochannel. Usually this process

is much quicker than that for the bulk diffusion along the x direction. Therefore, the ion transport in the y direction can be considered quasisteady state as shown in Fig. 2. It implies that the ion flux of the y component $\mathbf{J}_{y,i}$ is almost zero.

When we define $L_t = x^*$, the second relaxation time is $t_x^* = (x^*)^2/D_i$, denoting the time scale for bulk ion diffusion along the x direction, and the relationship between t_y^* and t_x^* is $t_y^*/t_x^* = \varepsilon^2$. Substituting $L_t = x^*$ into Eq. (7), we can obtain

$$\begin{aligned} \frac{\partial C_{i,0}}{\partial t_0} = & \left[\frac{\partial^2 C_{i,0}}{\partial x_0^2} + z_i \left(\frac{\partial C_{i,0}}{\partial x_0} \frac{\partial \psi_0}{\partial x_0} + C_{i,0} \frac{\partial^2 \psi_0}{\partial x_0^2} \right) \right] \\ & + \varepsilon^{-2} \left[\frac{\partial^2 C_{i,0}}{\partial y_0^2} + z_i \left(\frac{\partial C_{i,0}}{\partial y_0} \frac{\partial \psi_0}{\partial y_0} + C_{i,0} \frac{\partial^2 \psi_0}{\partial y_0^2} \right) \right]. \end{aligned} \quad (20)$$

Considering Eq. (19), the magnitude of the second term on the right side of Eq. (20) is

$$\begin{aligned} \varepsilon^{-2} \left[\frac{\partial^2 C_{i,0}}{\partial y_0^2} + z_i \left(\frac{\partial C_{i,0}}{\partial y_0} \frac{\partial \psi_0}{\partial y_0} + C_{i,0} \frac{\partial^2 \psi_0}{\partial y_0^2} \right) \right] \\ \sim O[\varepsilon^{-2} \exp(-\varepsilon^{-2})] \approx 0. \end{aligned} \quad (21)$$

Therefore Eq. (20) becomes

$$\frac{\partial C_{i,0}}{\partial t_0} = \frac{\partial^2 C_{i,0}}{\partial x_0^2} + z_i \left(\frac{\partial C_{i,0}}{\partial x_0} \frac{\partial \psi_0}{\partial x_0} + C_{i,0} \frac{\partial^2 \psi_0}{\partial x_0^2} \right). \quad (22)$$

From Eq. (20) to Eq. (22), we separate the two-dimensional ion transport process into several one-dimensional ion transport processes. It should be highlighted that this procedure is based on the assumption of quasisteady ion transport in the y direction, indicated by Eqs. (19) and (21).

Thus we decouple the two-dimensional ion transport equation, Eq. (7), into a steady-state ion distribution equation in the y direction, Eq. (19), and an unsteady-state ion transport equation along the x direction, Eq. (22). For a three-dimensional (3D) long, straight channel, the same scale transformations are applied, and the 3D dimensionless form is

similar to Eqs. (17), (19), and (22):

$$\frac{\partial^2 \psi_0}{\partial (y_0)^2} + \frac{\partial^2 \psi_0}{\partial (z_0)^2} = - \sum_i K_i^2 C_{i,m} \exp[-z_i(\psi_0 - \psi_{0,m})] z_i^{-1}, \quad (23)$$

$$\frac{\partial^2 C_{i,0}}{\partial y_0^2} + z_i \left(\frac{\partial C_{i,0}}{\partial y_0} \frac{\partial \psi_0}{\partial y_0} + C_{i,0} \frac{\partial^2 \psi_0}{\partial y_0^2} \right) = 0, \quad (24)$$

$$\frac{\partial^2 C_{i,0}}{\partial z_0^2} + z_i \left(\frac{\partial C_{i,0}}{\partial z_0} \frac{\partial \psi_0}{\partial z_0} + C_{i,0} \frac{\partial^2 \psi_0}{\partial z_0^2} \right) = 0, \quad (25)$$

$$\frac{\partial C_{i,0}}{\partial t_0} = \frac{\partial^2 C_{i,0}}{\partial x_0^2} + z_i \left(\frac{\partial C_{i,0}}{\partial x_0} \frac{\partial \psi_0}{\partial x_0} + C_{i,0} \frac{\partial^2 \psi_0}{\partial x_0^2} \right). \quad (26)$$

Therefore the process of ion electrodiffusion can be obtained by solving coupled equations (23)–(26) and these equations are named the upscaling PNP model. The major difference between the upscaling and the primary PNP model is the physical units of length along different directions, as shown in Fig. 3. In the primary PNP model, the resolution of length in the nanochannel is generally uniform grids and the length units use the same value y^* for the x and y directions [red square shown in Fig. 3(a)]. Most previous studies used such grids [53,54]. However, for the upscaling PNP model, the length units of the grids vary depending on need. More specifically, we use y^* (approximately nanometers) in the y direction and x^* (approximately millimeters or meters) in the x direction [blue square shown in Fig. 3(b)]. Another difference is that the time term in the upscaling PNP model is only dependent on the ion electrodiffusion along the x direction in Eq. (26). As already mentioned, the characteristic time for the ion transport in the primary PNP model is very small (about t_y^*) and therefore the time interval in the simulations should be small enough to meet the computing requirements. However, after the scale analysis, the characteristic time for the ion transport in the upscaling PNP model is t_x^* . Hence the time interval in the simulations is in the same magnitude with t_x^* . For example, if D uses the value of the real ion diffusivity, e.g., in the bulk water around $10^{-10} \text{ m}^2/\text{s}$, and the width and the length of a nanochannel are 10 nm and 10 cm, respectively, we define $y^* = 1 \text{ nm}$ so the characteristic time for the primary PNP model is $t = (y^*)^2/D = 10 \text{ ns}$. However, for the upscaling PNP model, $x^* = 1 \text{ cm}$ and the characteristic time for the same

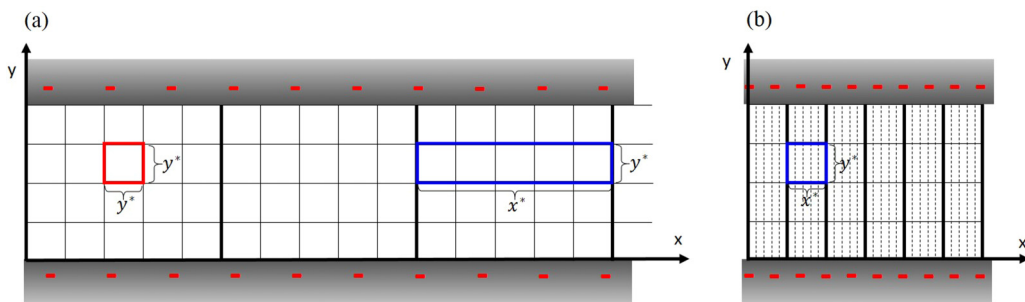


FIG. 3. The sketch of length scales in the primary PNP model (a) and upscaling PNP model (b). The uniform grids [red square in (a)] used by the primary PNP model have the same length scales for x and y directions, but grids [blue square in (b)] in the upscaling PNP model have unequal length scales. The blue square in (b) can be considered as the blue rectangle in (a).

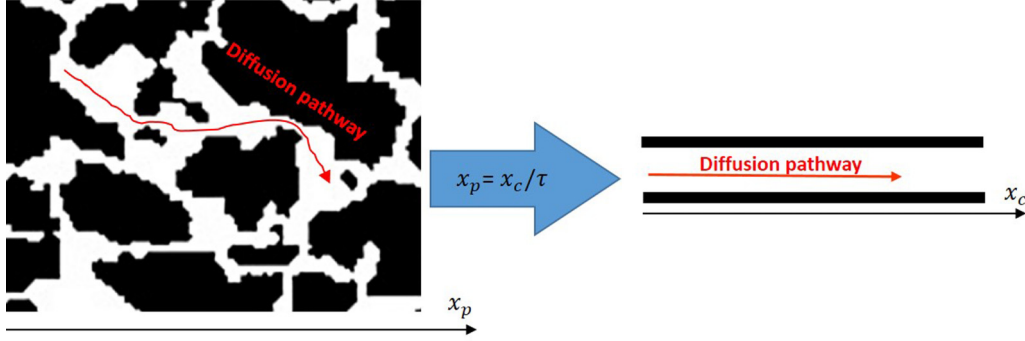


FIG. 4. The sketch of scale variations. Based on the tortuosity τ of the diffusion pathway, the position in the straight channel has a relationship ($x_p = x_c/\tau$) with that in the porous media. The red lines are the pathways of the ion diffusion. x_p is the x position for the porous media and x_c for the straight channel.

case is $t = (x^*)^2/D = 10^6$ s (0.032 year). Through this case, benefiting from the upscaling PNP model, the time scale is transformed from a nanosecond scale to a year scale.

B. Extension to porous media

The upscaling method in this work is straightforward for straight channels. Here we have to build a bridge from a straight channel to porous media. Considering the prior works by Bourg *et al.* [34] and Porta *et al.* [29], the transport process in porous media is equivalent to that comprising two infinite plates separated by a uniform aperture with a width \bar{d} in their works. Our model focuses on porous materials with homogeneous and isotropic properties (e.g., porosity or effective diffusivity). In the vision of the pore scale, it means that the pores or solid parts have their own equal probability to distribute everywhere in the domain with their fractions. For the concerned porous media, the width \bar{d} is usually the mean pore size calculated from the pore size distribution. Notice that the position in the porous media is not the same as it is in the channel because of the tortuous topology of the porous media. Shown in Fig. 4, it means the effective length for the ion diffusion in the porous media can be related to that in the channels by the concept of tortuosity, τ . The tortuosity is defined as the ratio of the average length $\langle L_T \rangle$ for the mass transport to the straight-line length L_s across the porous media [55]:

$$\tau = \frac{\langle L_T \rangle}{L_s}. \quad (27)$$

It is ambiguous for the average length $\langle L_T \rangle$, since it can change from one type of transport to another [55,56]. For the type of diffusion, there are several empirical correlations between the tortuosity and porosity found in the literature [55,57]. Because the porous morphology we were concerned with for ion diffusion is mostly granular, very similar to that in Delgado's work, we follow Delgado's model [57] to determine the value of tortuosity by

$$\tau = 1 - 0.5 \ln(\phi). \quad (28)$$

Considering $\varepsilon = y^*/x^*$ for the straight channel, this dimensionless spatial scale factor should be $\varepsilon = y^*/\langle L_T \rangle = y^*/\tau x^*$ for the porous media. Therefore, the time scale in the upscaling PNP model, $t_x^* = (x^*)^2/D_i$, for channels also becomes $t_x^* = (\tau x^*)^2/D_i$ for the porous media.

III. THE NUMERICAL MODEL AND ANALYSIS

A. Numerical methods

The set of dimensionless Poisson-Nernst-Planck equations subjected to the appropriate boundary conditions, derived by our upscaling analysis, is then solved by the coupled lattice Boltzmann (LB) codes [53,54,58]. The codes combine an ion diffusion evolution on discrete lattices to solve the dimensionless Nernst-Planck equation with a numerical solution for electric potential on the same set of lattices under the framework of the lattice Boltzmann method (LBM) to solve the nonlinear Poisson equation.

To solve the dimensionless Nernst-Planck equation, Eqs. (24)–(26), we use the following evolution equation [53,54,59]:

$$\begin{aligned} & g_\alpha^i(\mathbf{r} + \mathbf{e}_\alpha \delta_x, t + \delta_{t, D_i}) - g_\alpha^i(\mathbf{r}, t) \\ &= -\frac{1}{\tau_D} [g_\alpha^i(\mathbf{r}, t) - g_\alpha^{i, eq}(\mathbf{r}, t)], \end{aligned} \quad (29)$$

where \mathbf{r} denotes the position vector, and \mathbf{e}_α the discrete velocities, where $\alpha = 1, 2, \dots, N$ represents the discretized directions for a 3D seventh speed (D3Q7) system. The discretized directions for \mathbf{e}_α are shown in Fig. 5(a). We choose a consistent D3Q7 scheme for diffusion evolutions in this work, because this scheme is stable, accurate enough, and highly efficient for diffusion and electrical potential evolutions, compared with other schemes. For the D3Q7 lattice system of Eq. (29), the discrete velocities are

$$\mathbf{e}_\alpha = \begin{cases} (0,0,0) & \alpha = 0 \\ (\pm 1, 0, 0), (0, \pm 1, 0), (0, 0, \pm 1) & \alpha = 1 - 6 \end{cases}. \quad (30)$$

The equilibrium distribution function of the i th ion is

$$\begin{aligned} g_\alpha^{i, eq}(\mathbf{r}, t) = & \left[1 - 4 \frac{\delta_{t, i} z_i}{\delta_x} \left(\frac{\partial \psi_0}{\partial x_0} e_{x, \alpha} + \frac{\partial \psi_0}{\partial y_0} e_{y, \alpha} \right. \right. \\ & \left. \left. + \frac{\partial \psi_0}{\partial z_0} e_{z, \alpha} \right) \right] \omega_\alpha C_{i, 0}, \end{aligned} \quad (31)$$

with

$$\omega_\alpha = \begin{cases} 1/4 & \alpha = 0 \\ 1/8 & \alpha = 1 - 6 \end{cases}, \quad (32)$$

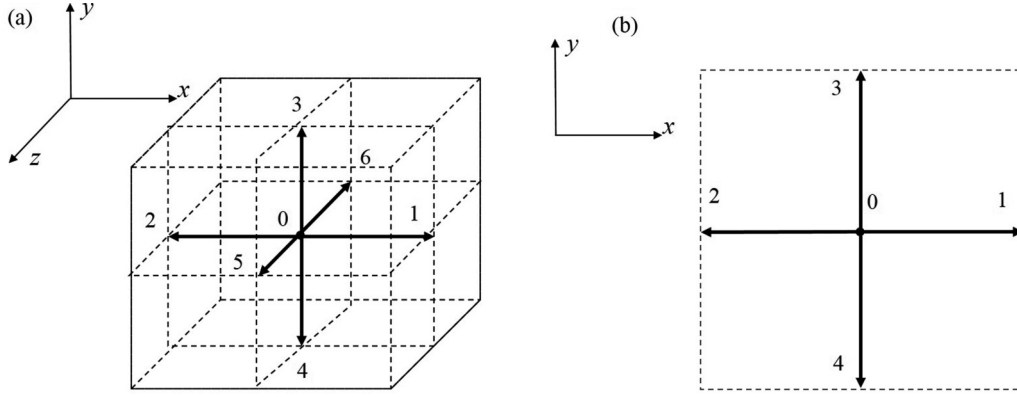


FIG. 5. The discretized directions in D3Q7 model (a) and D2Q5 model (b).

where τ_D is the dimensionless relation time and $\delta_{t,i}$ the corresponding dimensionless time step of the i th ion species.

The dimensionless relaxation time is calculated by

$$\tau_D = \frac{4}{c_D \delta_x} + \frac{1}{2}, \quad (33)$$

where c_D is the lattice speed for diffusion defined as $c_D = \delta_x / \delta_{t,i}$, with δ_x representing the lattice constant (dimensionless grid size). However, since the diffusivities of each ion are different, the time scales $t_x^* = (x^*)^2 / D_i$ are changing with the type of ions. Hence, we need to assign the same time step by adjusting τ_D for each ion. After evolutions, the macroscopic dimensionless ionic concentrations are calculated by

$$C_{i,0} = \sum g_\alpha^i. \quad (34)$$

To solve Eq. (23) under the framework of LBM, we construct the numerical evolution equation for electric potential distribution as [53]

$$h_\alpha(\mathbf{r} + \Delta \mathbf{r}, t + \delta_{t,\psi}) - h_\alpha(\mathbf{r}, t) = -\frac{1}{\tau_\psi} [h_\alpha(\mathbf{r}, t) - h_\alpha^{eq}(\mathbf{r}, t)] + \omega_\alpha \delta_{t,\psi} \frac{\rho_e}{\epsilon_r \epsilon_0}, \quad (35)$$

where τ_ψ is the dimensionless relaxation time for electric potential transport, c_ψ the dimensionless electrodynamic lattice speed defined as $c_\psi = \delta_x / \delta_{t,\psi}$, and $\delta_{t,\psi}$ the dimensionless time step.

Notice that the dimensionless Poisson equation (23) is two dimensional, because the gradient of potential along the x direction is negligible. For a D2Q5 lattice system, the equilibrium distribution of electric potential, h_α^{eq} , is

$$h_\alpha^{eq} = \begin{cases} \psi_0/3 & \alpha = 0 \\ \psi_0/6 & \alpha = 1 - 4 \end{cases}, \quad (36)$$

and the dimensionless relaxation time τ_ψ is calculated by

$$\tau_\psi = \frac{3}{c_\psi \delta_x} + \frac{1}{2}. \quad (37)$$

The macroscopic dimensionless electrical potential is then calculated by

$$\psi_0 = \sum h_\alpha. \quad (38)$$

The Dirichlet boundary condition is used for the electrical potential boundary on the solid surface [60]: $h_\alpha^i(\mathbf{r}, t + \delta_t) = -h_\beta^i(\mathbf{r}, t) + \zeta_0/3$, where the indices α and β are the opposite directions normal to the interface and β is the direction towards the boundary, ζ_0 the dimensionless zeta potential. For ion transport, the zero normal flux boundary condition is described as [54] $g_\alpha^i(\mathbf{r}, t + \delta_t) = g_\beta^i(\mathbf{r}, t)$. For the inlet and outlet boundary, the ion concentration in the diffuse layer matches with the Boltzmann distribution [52]: $C_{i,0} = C_{i,\infty} \exp(-z_i \psi_{0,\infty})$, where $C_{i,\infty}$ is the given dimensionless bulk ion concentration of inlet or outlet and $\psi_{0,\infty}$ the dimensionless electrical potential of the inlet or outlet. Then the Dirichlet boundary condition of ion concentration is used in the inlet or outlet as [60] $g_\alpha^i(\mathbf{r}, t + \delta_t) = -g_\beta^i(\mathbf{r}, t) + C_{i,0}/4$.

B. Validations

In this section, we verify the present upscaling method and LBM codes numerically. Several benchmarks are employed to model the steady and unsteady ion transport in a long, straight channel or porous media.

1. Long, straight channel case

First we consider steady-state ion diffusion in a two-dimensional (2D) nanochannel, as shown in Fig. 6, with a $0.585 \mu\text{m}$ width and $30 \mu\text{m}$ length. The main objective is to compare the ion concentration and electrical potential profiles simulated by the primary PNP model and the upscaling PNP model presented in this work. Define $y^* = 10 \text{ nm}$ and $x^* = 0.5 \mu\text{m}$. Therefore, the important parameter of the upscaling PNP model, dimensionless spatial scale factor ε , is chosen at $1/50$. The temporal scale ratio t_y^*/t_x^* should be consistent with the dimensionless spatial scale factor with the value $1/2500$. The electrolyte solution is NaCl solution and the bulk concentration is $1 \times 10^{-5} \text{ mol/l}$. For the steady state, the inlet and outlet ion concentration are given the same value as the bulk concentration. The other properties and physical parameters are as follows: The diffusion coefficients for both ions are $1.07 \times 10^{-10} \text{ m}^2/\text{s}$, the temperature 298.15 K , and the dielectric constant $6.95 \times 10^{-10} \text{ C}^2/\text{J m}$. We consider homogeneously charged surfaces, and the zeta potential for both walls is -50 mV . These parameter ranges are of interest in many engineering applications. The primary PNP model numerically solves the coupled Poisson-Nernst-Planck

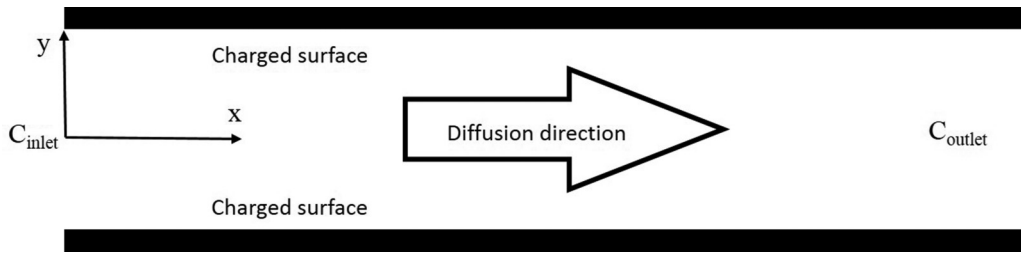


FIG. 6. Ion diffusion in microchannel. The black is the wall. The ionic concentration at inlet and outlet are given.

equations, Eqs. (2)–(4), that govern the ion transport with electrical double-layer effects. Therefore it can provide the reference calibration data for the upscaling PNP method. The primary PNP model adopts fine enough grids, i.e., 80×2000 uniform grids as shown in Fig. 3(a), while for the upscaling PNP model, a much coarser grid, an 80×40 grid, is used as shown in Fig. 3(b). We compare the steady electrical potential and ion concentration profiles in the cross sections of channels perpendicular to the x axis. Notice that the results in this section are given with real physical dimensions. Figure 7 shows good agreement between these two methods. As shown, the electrical potential exponentially decays with the distance away from the surface. The cations are converged and anions excluded near the negative charged surface because of the strong electrical interactions between ions and surfaces.

The transient ion transport process is a challenge for the prior upscaling methods because of the coupled interaction between the EDL and ion transport. It is difficult to build a bridge to make the communication from one scale to another scale. Therefore for the second step, we consider a transient case in the same nanochannel to test the capability of the upscaling scheme. For an unsteady state, the inlet and outlet ion concentration are 2×10^{-5} and 1×10^{-5} mol/l, respectively. The other physical parameters and mesh properties are the same as the first case above. Figure 8 shows the mean concentration along the nanochannel, comparing the upscaling PNP model with the primary PNP model. The ions diffuse from the inlet to the outlet, and the average concentration of cation is higher than that of anion owing to the electrical interactions. The figures show good agreement, which indicates our

upscaling method is able to deal with transient ion transport with multiple time scales.

2. Porous media case

For practicality, we further consider upscaling of ion diffusion in charged porous media. Here we use a two-dimensional simplified porous structure with a length of $36 \mu\text{m}$, as shown in Fig. 9. The solid phase is the gray circles with a radius of 30.4 nm . The porosity of the porous media is 0.8476 , and therefore the tortuosity is 1.1 calculated by Eq. (28). The mean pore size of this structure is $0.72 \mu\text{m}$ calculated by the maximum sphere method [61] and the zeta potential of the homogeneously charged surface for both models is -20 mV . The other physical parameters are the same as in the first case above. Two simulations are performed for the ion transport through the porous structure: One is the primary PNP model with a 81×2400 grid; the other is the upscaling PNP model with a 50×24 mesh. The space discretization depends on the balance between numerical accuracy and computational cost. For our upscaling model, the dimensionless spatial scale factor ε is $1/100$ in this simulation.

Figure 10 shows comparisons between both methods again for the ion concentration distributions at different times. Owing to the tortuous porous structure, the averaged ion concentrations obtained by the primary PNP method are fluctuating, while we can find that those modeled by the upscaling PNP method are within the fluctuations. The good agreement between the two methods indicates that the present upscaling method works well for upscaling of ion diffusion in

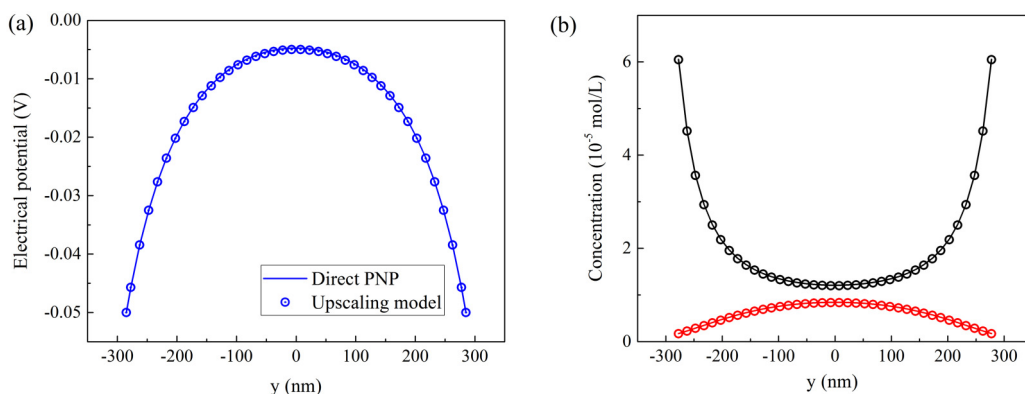


FIG. 7. The electrical potential profile of the cross section perpendicular to the x axis by the primary PNP model (solid line) and the upscaling PNP model (circle), shown in (a). Meanwhile the ion concentration profile is shown in (b): the red is for anions and the black, for cations.

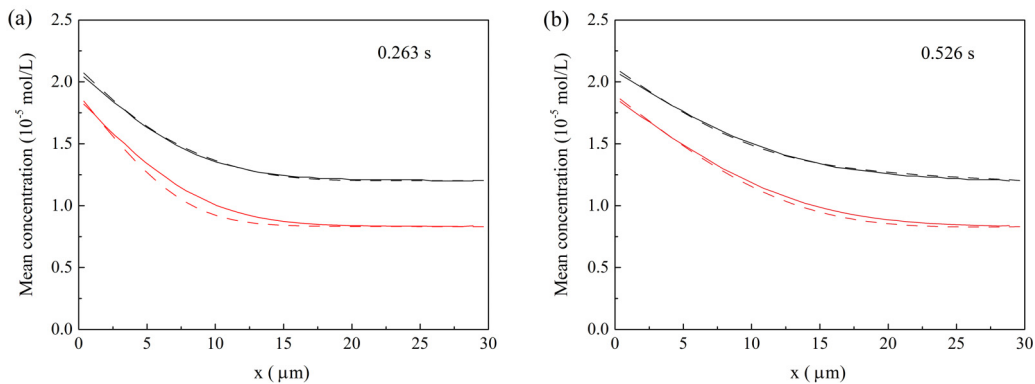


FIG. 8. The mean concentration in the nanochannel along the diffusion direction. The diffusion times are 0.263 s (a) and 0.526 s (b). The red represents anions and the black, cations. The dotted line is the result from the upscaling PNP model and solid line primary PNP model.

charged porous media. For efficiency concerns, the primary PNP scheme on the full-size fine grid used about 1 month while the upscaling scheme only cost several hours on the same computing resources (Intel Xeon CPU E5-2650, 2.60 GHz).

3. Comparisons with experimental data

After validations by comparisons with the full solutions of the primary PNP model in straight channels and simplified porous media, we want to demonstrate the robust capability of the upscaling model by experimental data of realistic physical problems. In geoenvironmental engineering, bentonites have shown the potential as the buffer material for nuclear waste disposal. The bentonite is generally a composite formed by two or more types of clays (e.g., morillonite, illite, and kaolinite, etc.). To understand the mechanism of ion transport in such complex material, experiments in compacted bentonite have been performed using throughdiffusion, outdiffusion, and concentration profile analysis techniques in the previous studies [12,14], which measured the apparent diffusion coefficients and the capability of adsorptions for radioactive

tracers in compacted bentonites. These experiments are typically time and money consuming [62] and the experimental data with open access was very rare, because usually the experiment duration is about tens of days or months. Numerical simulations therefore provide an ecofriendly and effective method. Especially, the upscaling modeling is more efficient; for example, simulations based our upscaling PNP model cost only a few hours for a typical case.

First we compare our predictions of the ion throughdiffusion flux by time in the hardened cement pastes with the measured data by Tits *et al.* [63]. Their experiments used $^{22}\text{Na}^+$ as the ion tracers diffusing through the hardened cement pastes (a charged porous media) with a length of 10 cm. Our upscaling method uses a 44×100 grid and the dimensionless spatial scale factor is 1.98×10^{-6} . The zeta potential for the cement paste is -20 mV, which is a common value for the general cement pore solution. We also consider a case with zero zeta potential as a special case without EDL effects for contrast. The experiments by Tits adopted an artificial cement pore solution with the components of 0.426 g/l Na_2SO_4 and 6.65×10^{-3} g/l AlCl_3 . Additionally,

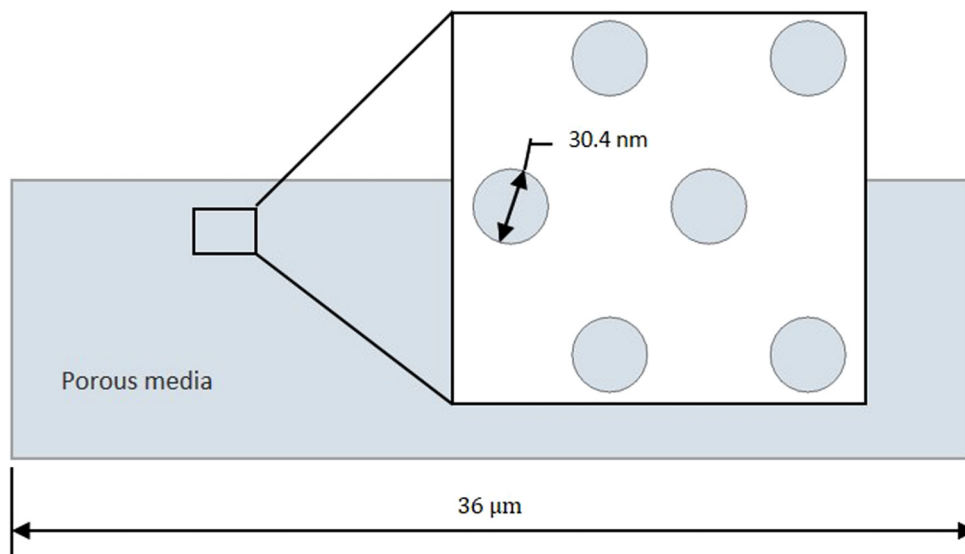


FIG. 9. A sketch of the porous media for the simulation domain.

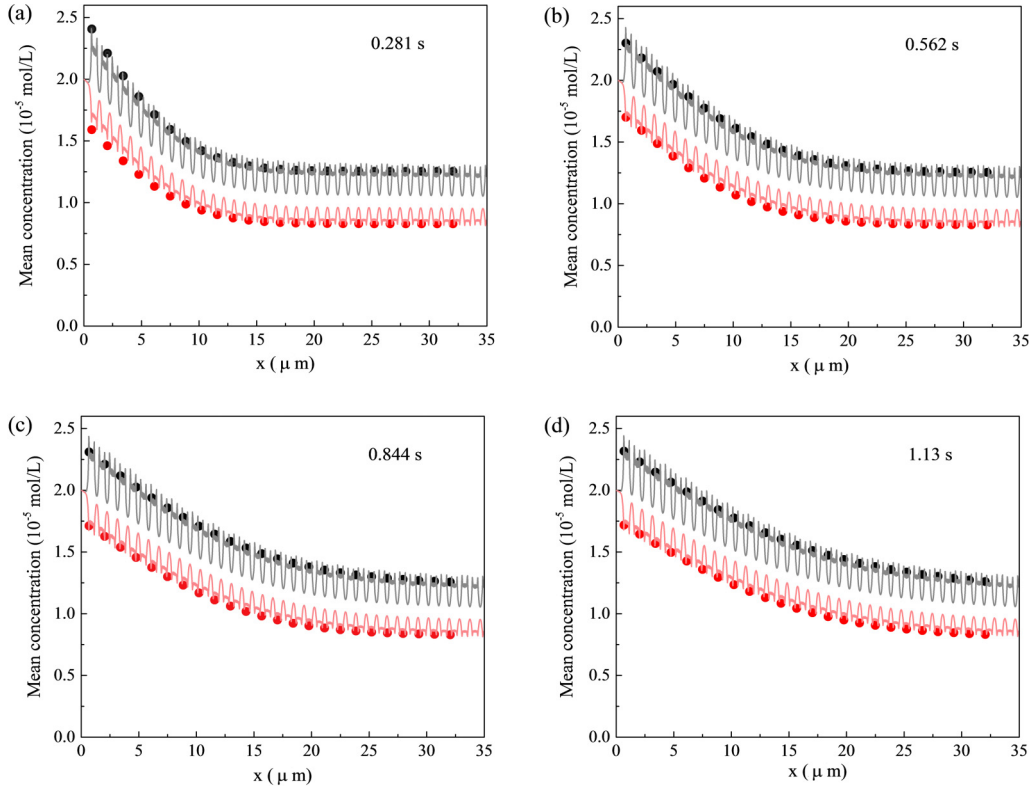


FIG. 10. The mean concentration of the cross section in the porous media on different x position. Four diffusion times are chosen: 0.281, 0.562, 0.844, and 1.13 s. The red represents anions and black, cations. The circles are the results from the upscaling PNP model and solid line primary PNP model.

we used the real ionic diffusion coefficients in the bulk water, i.e., $D_{Na^+} = 1.33 \times 10^{-9} \text{ m}^2/\text{s}$, $D_{SO_4^{2-}} = 1.06 \times 10^{-9} \text{ m}^2/\text{s}$, $D_{Al^{3+}} = 0.54 \times 10^{-9} \text{ m}^2/\text{s}$ and $D_{Cl^-} = 2.03 \times 10^{-9} \text{ m}^2/\text{s}$, in our modeling.

Following the experiment, we use the artificial cement pore solution as the inlet and outlet boundary conditions. As the steady-state ion distributions achieved, the tracer ions are added at the inlet so that the numerical inlet concentration condition is a Dirichlet boundary at $3.6 \times 10^{-9} \text{ mol/l } ^{22}\text{NaCl}$. As a result, the tracer ions, $^{22}\text{Na}^+$, will diffuse from inlet to outlet by the concentration gradient. In this experiment, the hardened cement pastes with a water to cement ratio of 1:3 hydrated for 6 months. Based on the Hansen’s theory [64] the porosity ϕ of this cement paste is calculated as 0.075. The tortuosity is also given by Eq. (28) as 3.0. Meanwhile the ion flux given by our upscaling method is

$$J_{i,\text{cement}} = J_{i,\text{channel}} \phi, \quad (39)$$

which means that the porosity bridges the ion flux between channels and porous media. We calculate the $^{22}\text{Na}^+$ diffusion flux versus time at the outlet by our prediction and compare the results with experiment data [63]. Figure 11 shows the good agreement of our upscaling predictions with the experiment data. Meanwhile, the results indicate that the $^{22}\text{Na}^+$ flux may be significantly underestimated if the EDL (electrical double-layer effect) is ignored.

When the diffusion is steady and the flux is changeless, as shown on the right side of Fig. 11, the outdiffusion test is applicable. At this time, the difference of tracer-ion

concentrations at inlet and outlet vanishes. For the outdiffusion test, the tracer-ion concentrations are set at zero at both ends when the test starts. The tracer ions diffuse from inside to outside and the ion flux can be calculated over time at both ends by the upscaling predictions. Figure 12 compares the numerical results with the experiment data, where the

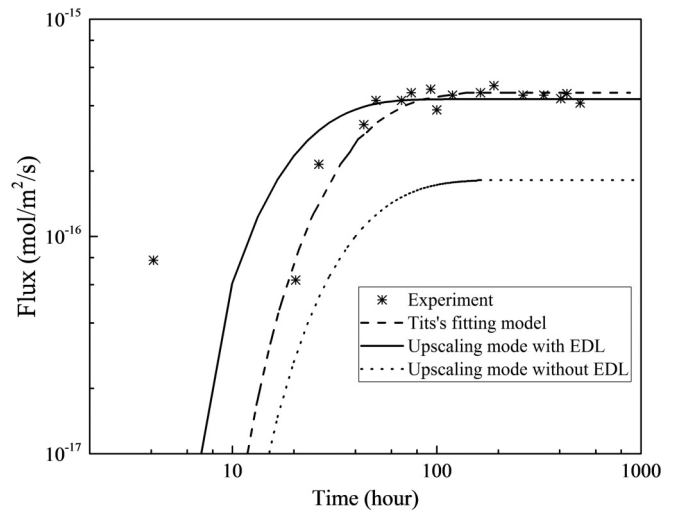


FIG. 11. The throughdiffusion results of experiment data (star points), the best fitting model (dashed line) from the literature by Tits [63], our upscaling model with EDL (solid line), and without EDL (dot line).

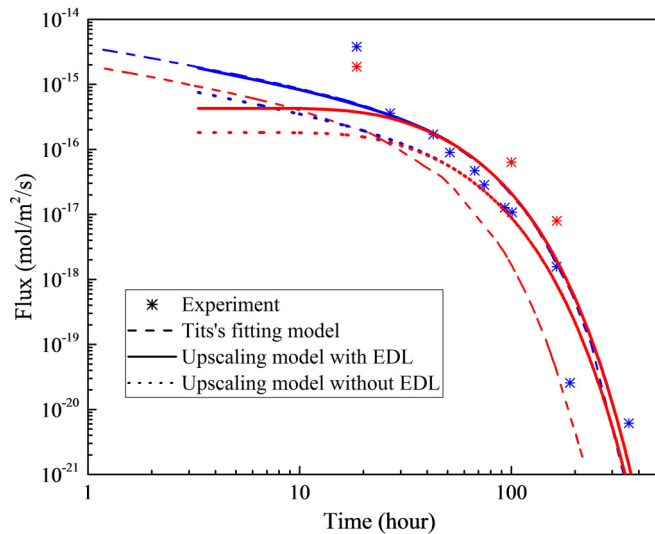


FIG. 12. The outdiffusion results of experiment data, fitting model from the literature by Tits [63], our upscaling model with EDL and without EDL. The blue is the flux at the inlet and the red is at the outlet.

agreement is good. In both Figs. 11 and 12, we also plot the corresponding Tits's fitting models in the same cases. The agreement of the fitting models with the experimental data is also not bad, but the fitting parameters are not predictable and have to be determined case by case. All the parameters in the present upscaling model have clear physical meaning, which ensures that it is capable of catching the long-term ion diffusion mechanism in charged porous media. Again the ionic flux is underrated by the predictions without EDL shown in Fig. 12, which confirms again that the electrical double-layer effect has a remarkable influence on ion diffusion.

IV. CONCLUSIONS

We present here an upscaling framework to study long-term ion diffusion with electrical double-layer effects in charged porous media. After the scale analysis of dimensionless PNP equations, we decouple the PNP equations for different

directions and separate the coupled two-dimensional ion transport process into several one-dimensional ion transport processes. Therefore we use apposite temporal and spatial scales for corresponding directions. With these treatments, we have the ability to deal with long-term problems for the ion transports with electrical double-layer effects. The Donnan theory used by previous studies is a consequence of Poisson's equation when the ratio of a Debye length and the characteristic size of pores is small. However, this upscaling model is directly based on the assumption of the Poisson-Boltzmann equilibrium in the directions orthogonal to transport. Hence it can deal with a wider range of pore size and more complex electrolytes compared with previous approaches. Our upscaling method is solved by a high-efficiency coupled lattice Boltzmann method. In order to validate our upscaling scheme, we compare the calculated concentration profiles of ion diffusion in a long, straight channel or simplified porous media with the full solutions by the primary PNP model for both steady and unsteady cases. Good accuracy of the present model is proved and the efficiency is significantly improved. Then the upscaling method is used to predict the tracer-ion diffusion in hardened cement pastes and compared with the experimental data for both throughdiffusion and outdiffusion cases. The good agreement indicates the robustness of our method again. All parameters in the present model have clear physical meaning and no fitting parameters are needed, which ensures that it is capable of real prediction and to reveal the physics and mechanism of ion transport in charged porous media. The proposed upscaling scheme may build a bridge from the pore scale to the Darcy scale, especially for the long-term behavior of ion transport. Meantime this scheme also provides a potential solution for other similar mass, heat, or momentum coupled transport process.

ACKNOWLEDGMENTS

This work is financially supported by the NSF Grant of China (Grants No. 51676107 and No. 91634107) and National Science and Technology Major Project on Oil and Gas (Grant No. 2017ZX05013001).

- [1] H. B. Bradl, *J. Colloid Interface Sci.* **277**, 1 (2004).
- [2] A. Ontiveros-Ortega, F. Vidal, E. Gimenez, and J. Ibáñez, *J. Mater. Sci.* **49**, 3550 (2014).
- [3] C. Zhang, A. Revil, Y. Fujita, J. Munakata-Marr, and G. Redden, *Geophysics* **79**, D363 (2014).
- [4] F. Bazer-Bachi, M. Descostes, E. Tevissen, P. Meier, B. Grenut, M. O. Simonnot, and M. Sardin, *Phys. Chem. Earth* **32**, 552 (2007).
- [5] A. W. Miller and Y. Wang, *Environ. Sci. Technol.* **46**, 1981 (2012).
- [6] K. M. Sample-Lord and C. D. Shackelford, *J. Geotech. Geoenviron. Eng.* **142**, 04016033 (2016).
- [7] H. Friedmann, O. Amiri, and A. Ait-Mokhtar, *Cem. Concr. Res.* **38**, 1394 (2008).
- [8] M. Manera, O. Vennesland, and L. Bertolini, *Corros. Sci.* **50**, 554 (2008).
- [9] B. Šavija, M. Luković, and E. Schlangen, *Cem. Concr. Res.* **61-62**, 49 (2014).
- [10] Z. Song, L. Jiang, J. Liu, and J. Liu, *Constr. Build. Mater.* **99**, 150 (2015).
- [11] M. Aguayo, P. Yang, K. Vance, G. Sant, and N. Neithalath, *Cem. Concr. Res.* **66**, 1 (2014).
- [12] M. A. Glaus, S. Frick, R. Rossé, and L. R. V. Loon, *Geochim. Cosmochim. Acta* **74**, 1999 (2010).
- [13] C. D. Shackelford and S. M. Moore, *Eng. Geol.* **152**, 133 (2013).
- [14] Y. Tachi and K. Yotsuji, *Geochim. Cosmochim. Acta* **132**, 75 (2014).
- [15] M. A. Glaus, M. Aertsens, C. A. J. Appelo, T. Kupcik, N. Maes, L. Van Laer, and L. R. Van Loon, *Geochim. Cosmochim. Acta* **165**, 376 (2015).
- [16] T. Gimmi and G. Kosakowski, *Environ. Sci. Technol.* **45**, 1443 (2011).

- [17] C. A. J. Appelo and P. Wersin, *Environ. Sci. Technol.* **41**, 5002 (2007).
- [18] D. Jougnot, A. Revil, and P. Leroy, *Geochim. Cosmochim. Acta* **73**, 2712 (2009).
- [19] H. Daigui, P. Yang, and A. Majumdar, *Nano Lett.* **4**, 137 (2004).
- [20] F. H. J. van der Heyden, D. Stein, and C. Dekker, *Phys. Rev. Lett.* **95**, 116104 (2005).
- [21] M. Wang and S. Chen, *J. Colloid Interface Sci.* **314**, 264 (2007).
- [22] M. Wang, Q. Kang, H. Viswanathan, and B. A. Robinson, *J. Geophys. Res.* **115**, B10205 (2010).
- [23] A. L. Morancho, M. V. Villar, M. Sanchez, A. G. Solé, X. P. Llurba, and E. A. Pérez de Agreda, *Géotechnique* **53**, 27 (2003).
- [24] I. Sondi, J. Bišćan, and V. Pravdić, *J. Colloid Interface Sci.* **178**, 514 (1996).
- [25] M. Mullet, P. Fievet, J. C. Reggiani, and J. Pagetti, *J. Membr. Sci.* **123**, 255 (1997).
- [26] P. Leroy and A. Revil, *J. Colloid Interface Sci.* **270**, 371 (2004).
- [27] I. Rubinstein, B. Zaltzman, A. Futerman, V. Gitis, and V. Nikonenko, *Phys. Rev. E* **79**, 021506 (2009).
- [28] M. Z. Bazant, K. Thornton, and A. Ajdari, *Phys. Rev. E* **70**, 021506 (2004).
- [29] G. Porta, B. Bijeljic, M. Blunt, and A. Guadagnini, *Geophys. Res. Lett.* **42**, 7537 (2015).
- [30] T. Kozaki, A. Fujishima, S. Sato, and H. Ohashi, *J. Nucl. Technol.* **121**, 63 (1998).
- [31] M. Tyagi, T. Gimmi, and S. V. Churakov, *Adv. Water Resour.* **59**, 181 (2013).
- [32] A. Obliger, M. Jardat, D. Coelho, S. Bekri, and B. Rotenberg, *Phys. Rev. E* **89**, 043013 (2014).
- [33] S. Li, A. Raouf, and R. Schotting, *J. Hydrol.* **517**, 1107 (2014).
- [34] I. C. Bourg, G. Sposito, and A. Bourg, *Clays Clay Miner.* **54**, 363 (2006).
- [35] U. M. B. Marconi and S. Melchionna, *Mol. Phys.* **111**, 3493 (2013).
- [36] E. Samson, J. Marchand, and J. J. Beaudoin, *Cem. Concr. Res.* **29**, 1341 (1999).
- [37] S. Scheiner, P. Pivonka, and D. W. Smith, *Comput. Geotech.* **48**, 283 (2013).
- [38] E. Lemarchand, C. A. Davy, L. Dormieux, W. Chen, and F. Skoczylas, *Transp. Porous Media* **79**, 335 (2009).
- [39] S. A. de Lima, M. A. Murad, C. Moyne, and D. Stemmelen, *Transp. Porous Media* **85**, 23 (2010).
- [40] C. Moyne and M. A. Murad, *Int. J. Solids Struct.* **39**, 6159 (2002).
- [41] P. Leroy, A. Revil, and D. Coelho, *J. Colloid Interface Sci.* **296**, 248 (2006).
- [42] P. Pivonka, D. Smith, and B. Gardiner, *Transp. Porous Media* **69**, 215 (2007).
- [43] S. M. Rubinstein, G. Manukyan, A. Staicu, I. Rubinstein, B. Zaltzman, R. G. H. Lammertink, F. Mugele, and M. Wessling, *Phys. Rev. Lett.* **101**, 236101 (2008).
- [44] E. A. Demekhin, V. S. Shelistov, and S. V. Polyanskikh, *Phys. Rev. E* **84**, 036318 (2011).
- [45] T. A. Zangle, A. Mani, and J. G. Santiago, *Langmuir* **25**, 3909 (2009).
- [46] H. Tian, L. Zhang, and M. Wang, *J. Colloid Interface Sci.* **452**, 78 (2015).
- [47] A. Revil and P. Leroy, *J. Geophys. Res., [Solid Earth Planets]* **109**, 208 (2004).
- [48] R. K. Iler, *The Chemistry of Silica: Solubility, Polymerization, Colloid and Surface Properties, and Biochemistry* (Wiley, New York, 1979).
- [49] C. C. Lin and L. A. Segel, *Mathematics Applied to Deterministic Problems in the Natural Sciences* (Society for Industrial and Applied Mathematics, Philadelphia, 1988), p. 185.
- [50] K. Rodríguez and M. Araujo, *J. Colloid Interface Sci.* **300**, 788 (2006).
- [51] *Irreversible Systems, Colloid Science* Vol. I, edited by H. R. Kruyt, English translation, L. C. Jackson (Elsevier, Amsterdam, 1952).
- [52] M. Wang and S. Chen, *Commun. Comput. Phys.* **3**, 1087 (2008).
- [53] M. Wang and Q. Kang, *J. Comput. Phys.* **229**, 728 (2010).
- [54] H. Yoshida, T. Kinjo, and H. Washizu, *Commun. Nonlinear Sci. Numer. Simul.* **19**, 3570 (2014).
- [55] B. Ghanbarian, A. G. Hunt, R. P. Ewing, and M. Sahimi, *Soil Sci. Soc. Am. J.* **77**, 1461 (2013).
- [56] F. J. Valdés-Parada, M. L. Porter, and B. D. Wood, *Transp. Porous Media* **88**, 1 (2010).
- [57] J. M. P. Q. Delgado, *Can. J. Chem. Eng.* **84**, 651 (2008).
- [58] M. Wang and Q. Kang, *Anal. Chem.* **81**, 2953 (2009).
- [59] L. Zhang and M. Wang, *J. Geophys. Res., [Solid Earth Planets]* **120**, 2877 (2015).
- [60] H. Yoshida and M. Nagaoka, *J. Comput. Phys.* **229**, 7774 (2010).
- [61] S. Bhattacharya and K. E. Gubbins, *Langmuir* **22**, 7726 (2006).
- [62] C. L. Chen, T. H. Wang, C. H. Lee, and S. P. Teng, *J. Contam. Hydrol.* **138-139**, 1 (2012).
- [63] J. Tits, A. Jakob, E. Wieland, and P. Spieler, *J. Contam. Hydrol.* **61**, 45 (2003).
- [64] T. C. Hansen, *Mater. Struct.* **19**, 423 (1986).